High lithium oxide prevalence in the lithium solid electrolyte interphase drives high Coulombic efficiency

Betar M Gallant

bgallant@mit.edu

MIT https://orcid.org/0000-0002-4586-2769

Gustavo Hobold

MIT

Chongzhen Wang

University of California, Los Angeles

Katherine Steinberg

Massachusetts Institute of Technology https://orcid.org/0000-0002-8232-7714

Yuzhang Li

University of California, Los Angeles https://orcid.org/0000-0002-1502-7869

Article

Keywords:

Posted Date: August 2nd, 2023

DOI: https://doi.org/10.21203/rs.3.rs-3203979/v1

Additional Declarations: There is **NO** Competing Interest.

Version of Record: A version of this preprint was published at Nature Energy on April 8th, 2024. See the published version at https://doi.org/10.1038/s41560-024-01494-x.

Abstract

Current electrolyte design for Li metal anodes emphasizes fluorination as the guiding principle for high Coulombic efficiency (CE) based largely on perceived benefits of LiF in the solid electrolyte interphase (SEI). However, the lack of experimental techniques that can accurately quantify SEI compositional breakdown impedes rigorous scrutiny of other potentially key phases. Here we demonstrate a new quantitative titration approach to reveal Li_2O content in cycled Li anodes, enabling this previously titration-silent phase to be compared statistically with a wide range of other leading SEI constituents including LiF. Across diverse electrolytes, Li_2O correlates most strongly with CE above other phases, reaching highest values when Li_2O particles order along the SEI-electrolyte interface as revealed by cryo-TEM, demonstrating integrated chemical–structural function. The beneficial role of Li_2O was exploited to create a first set of entirely fluorine-free electrolytes to breach > 99% CE, highlighting electrolyte/SEI oxygenation as an underexplored and powerful design strategy.

Introduction

Replacing the graphite anode in Li-ion batteries with Li metal is one of the most compelling strategies to meet targets of > 750 Wh/L for electric vehicles,[2,3] but Li cannot yet achieve Coulombic efficiencies (CE) > 99.95% required for > 1,000 cycle life.[4–6] During cycling, active Li inventory is lost to several pathways: (1) As solubilized material at ultralow CE (< ~ 10%); (2) Evolution of electronically isolated Li^0 at intermediate CE (~ 10–95%); and (3) Irreversible formation of the solid electrolyte interphase (SEI), which dominates losses as CE reaches 99%.[6–8] To support design of very high-CE electrolytes, it is becoming crucial to understand the ideal target SEI composition and gain precise control over SEI formation so that only the most beneficial phases are formed.

Even after extensive research, SEI chemical and functional understanding is remarkably incomplete and reliant upon qualitative models.[9,10] Broadly, it is accepted that the SEI comprises inorganic and organic phases, with the former including lithium fluoride (LiF), lithium oxide (Li_2O), lithium carbonate (Li_2CO_3), and lithium nitride (Li_3N) depending on salt; and the latter including semicarbonates ($ROCO_2Li$), alkoxides (ROLi), and poly/oligomers depending on solvent.[11] More accurately determining SEI composition remains a major challenge due to its exceedingly low amounts (sub-$\mu mol_{Li}/cm^2$/cycle at > 99% CE), instability and susceptibility to contamination during analysis, and limitations of spectroscopy techniques. Much understanding derives from X-ray photoelectron spectroscopy (XPS),[10] which has low depth sensitivity (~ 10 nm), resulting in widespread use of sputter depth-profiling that can create compositional artifacts like fictitious LiF enrichment[12–14] from beam-induced decomposition of electrolyte salts and fragments.

Despite this, LiF has been proposed as a leading SEI descriptor, resulting in electrolyte fluorination becoming the principal electrolyte design strategy (**Supplementary Fig. 1**).[15–18] Based on bulk properties, LiF has been rationalized to be a desirable SEI phase given its chemical inertness, mechanical strength,

low electronic conductivity, and high interfacial energy.[17] Yet it is unclear whether bulk properties are relevant in the nanoscopic, complex SEI, and LiF is among the more resistive phases for Li^+ transport.[19–22] Additionally, mounting evidences suggest that LiF has no clear chemical benefit in the SEI,[17,22,23] instead playing the role of an inert building block, and raising the question as to which phases provide the major SEI functionality.

Lithium oxide (Li_2O) is the second major ionic phase present in all model descriptions of the SEI[10,11] but has received less focus. We previously observed that nanostructured Li_2O on Li possesses a ~ 2× higher Li^+ conductivity than LiF, which can support more homogeneous Li^+ flux, rendering Li_2O more beneficial to SEI transport.[19] This hypothesis is consistent with observed O-enrichment of many high–CE SEI[24,25] and in some advanced electrolytes.[26,27] Weighing the relative significance of Li_2O, LiF and other phases is however challenging without an ability to accurately determine their relative proportions throughout the SEI. Titration-based analysis of cycled electrode materials has emerged in recent years as a powerful technique to quantify inactive Li^0 and a growing number of SEI phases,[8,28–31] but the lack of a Li_2O-selective technique appropriate for cycled Li anodes has left Li_2O as a titration-silent phase. Salt-derived phases like Li_3N, S- and B-containing phases have also not yet been quantified.

To fill this gap, this work reports an alcohol-based titration followed by Karl-Fischer analysis that selectively quantifies total Li_2O in cycled Li anodes. The method is integrated into a broader workflow designed to quantify other key SEI phases in parallel—LiF, Li_3N, S-, P-, B-containing phases, $ROCO_2Li$, Li_2C_2, RLi—as well as inactive Li^0, providing a methodology to probe the rich SEI composition and resolve the key building blocks in the limit of high CE. Across ten diverse electrolytes spanning broad composition and CE range, a major fraction of capacity loss is allocated, substantially exceeding prior quantification benchmarks.[7] Contrary to conventional understanding, Li_2O is the most consistently abundant phase at high CE and the strongest CE descriptor, surpassing LiF, even in highly fluorinated electrolytes. Cryogenic high resolution transmission electron microscopy (Cryo-HRTEM) characterization further reveals that the distribution of Li_2O within the SEI affects CE, providing both chemical and morphological function. Leveraging these findings, we demonstrate the possibility to achieve highly competitive > 99% CE using oxygenated, rather than fluorinated, solvents and salts. The results indicate that LiF enrichment is not strictly requisite for high CE and highlight SEI oxygenation as a compelling but underexplored pathway to expand versatility of electrolyte design.

Quantitative titration of Li_2O in cycled anodes

Samples for titration analysis were generated over several plating/stripping cycles of Li on Cu to accumulate irreversible materials (herein termed SEI/Li^0 residuals), ending with a full stripping step. The Li_2O titration (Fig. 1a) is a two-step reaction in which residuals on Cu are reacted with 2-butoxyethanol to form LiOH from any present Li_2O ($Li_2O + BuOC_2H_4OH \rightarrow LiOH + BuOC_2H_4OLi$).[32,33] The LiOH solution is injected into a Karl Fischer (KF) titrator and reacted to completion (**Supplementary Fig. 2**). LiOH is

detected as H_2O and related back to the original amount of SEI Li_2O by charge balance (2 e^- detected at the KF electrode per unit LiOH = unit Li_2O; Fig. 1b). The 2-butoxyethanol/KF titration series is selective to Li_2O and LiOH over other SEI phases such as Li_2CO_3, Li_3N, LiH, LiF, as well as metallic Li^0 (Fig. 1c). The latter reacts with 2-butoxyethanol to form an alkoxide rather than LiOH, thus is invisible to KF titration.[33] In this regard, using alcohol as the titrant provides an important advantage over acid-base titration of Li_2O,[34] because aqueous titrations yield LiOH from both Li_2O and Li^0, which cannot be differentiated (**Supplementary Note 1**). LiOH was confirmed to be insignificant in the initial SEI using ATR-IR spectroscopy and low water-content electrolytes (**Supplementary Figs. 3–4, Supplementary Note 2**), thus only formed upon butoxyethanol reaction with SEI Li_2O.

The Li_2O titration was integrated into a parallelized workflow to quantify capacity loss partitioning in a first exemplar electrolyte, 1 M $LiPF_6$ in EC/DEC (50/50 vol%), examined previously by titration but with no information on Li_2O.[7] A three-pronged titration scheme was adopted wherein batches of Cu/Li cells were cycled galvanostatically to a targeted capacity loss and diverted to either HCl, water, or 2-butoxyethanol titration (**Supplementary Figs. 5–7)**. Following prior work,[7] the first two are used to quantify inactive Li^0, $ROCO_2Li$, Li_2C_2, RLi (HCl) and LiF, P-containing phases (H_2O). Samples used for those titrations were rinsed with anhydrous DMC to remove electrolyte, which was confirmed not to alter the detected SEI composition or amount of Li^0 (**Supplementary Fig. 8**). The targeted capacity loss was ~ 1 mAh for acid/water and ~ 2 mAh for butoxyethanol, determined by minimum sample requirements for limiting phases in each method (**Supplementary Fig. 9**).

Titration results (Fig. 1d) were normalized to each cell's capacity loss and averaged across replicates, yielding the capacity loss partitioning (%) of the electrolyte shown in Fig. 1e (**Supplementary Methods**). As observed previously,[7] a major capacity loss mechanism in 1 M $LiPF_6$ EC/DEC forms inactive Li^0 (46.1% of total loss). However, among the remaining 53.9% comprising SEI phases, strong Li_2O prevalence could be confirmed for the first time (yellow bars). Moreover, Li_2O was the most abundant detectable SEI phase (15.4% of total loss or 28.6% of SEI Li^+), followed more remotely by $ROCO_2Li$ (4.8% and 8.9%, respectively) and yet-more minor phases: RLi, Li_2C_2, P-containing phases, and LiF, each comprising < 1% of total capacity loss. The remaining unidentified SEI losses (~ 32%) correspond to solvent-derived or soluble phases that currently elude titration analysis. To better understand the relationship between SEI composition and performance, the workflow is next applied to a broader series of electrolytes.

Li_2O and SEI quantification across diverse electrolytes

A range of electrolyte compositions, spanning carbonate/ether classes and diverse salts, were selected to bridge low to high CE (Fig. 2a, Table 1). To account for different salt products (Fig. 2b), S- and B-containing phases were quantified by ICP-AES and Li_3N was analyzed by a salicylate assay method[35] in addition to the above-noted workflow, after cells were cycled to their target capacity loss over 1–10

cycles. Figure 2c shows the compositional breakdowns by rank in select electrolytes, with the complete data for all electrolytes in Fig. 2d (titration data: **Supplementary Figs. 10–23**, **Supplementary Tables 1–7**; SEI breakdown: **Supplementary Fig. 24**). Key findings in each electrolyte are first highlighted prior to a cross-comparison by phase.

Table 1
Summary of analyzed electrolytes, CEs measured from the galvanostatic cycling protocols used for each electrolyte (**Supplementary Table 3**), and Li_2O and LiF contents. Information on other phases can be found in **Supplementary Table 7**. Abbreviated electrolyte nomenclatures are defined in **Supplementary Methods**.

Electrolyte	CE (%)	Li_2O (%[1])	LiF (%[1])
1.37 M LiTFSI 7TTE/3DMC (70/30 vol%)	40.7	1.1	0.41
1 M LiTFSI DOL/DME (50/50 vol%)	59.8	4.9	0.80
1.37 M LiFSI 5TTE/5DMC (50/50 vol%)	75.1	4.4	2.60
1 M $LiPF_6$ EC/DEC (50/50 vol%) + 10vol% VC	89.9	7.0	2.40
1 M $LiPF_6$ EC/DEC (50/50 vol%)	92.6	14.6	0.18
1 M $LiPF_6$ EC/DEC (50/50 vol%) + 10vol% FEC	95.1	26.4	3.81
1.2 M $LiBF_4$ 1FEC/2DEC (33/66 vol%)	95.9	26.1	14.54
0.6 M $LiBF_4$ 0.6 M LiDFOB 1FEC/2DEC (33/66 vol%)	97.3	33.2	12.95
1.37 M LiFSI 7TTE/3DMC (70/30 vol%)	98.6	24.9	13.07
1 M LiTFSI DOL/DME (50/50 vol%) + 3wt% $LiNO_3$	98.7	80.8	4.28

[1] Indicated Li_2O and LiF amounts are normalized to the irreversible capacity loss.

A first electrolyte examined was 1.37 M LiTFSI in 7TTE/3DMC (CE = 40.7%). Expectedly for very low CE, capacity loss was dominated by Li^0 (81.9% of total loss).[8] The SEI comprised S-containing phases from LiTFSI followed by minor Li_2O/LiF. Organofluorine (R-CF_x) species, consistent with $TFSI^-$/TTE decomposition, were also observed by ^{19}F-NMR (**Supplementary Fig. 25**; **Supplementary Figs. 26–34** for other electrolytes), though could not be quantified due to unknown fluorine stoichiometry *x*. Upon changing the solvent (1 M LiTFSI in DOL/DME), CE increased (59.8%), Li^0 decreased and Li_2O increased, though was still relatively minor. While S- and F-containing phases in this electrolyte arise unambiguously from salt decomposition, Li_2O could also form from solvent reduction. Notably, this electrolyte yields the largest proportion of unresolved phases (gray region, 44.8% of total capacity loss) consistent with an organics-dominated SEI.[36] A third electrolyte replaces LiTFSI with LiFSI and achieves higher CE (1.37 M LiFSI 5TTE/5DMC, CE = 75.1%) and a higher SEI proportion of S-containing phases (35.8% of capacity loss) from stronger participation of FSI^- in SEI formation. Li_2O and LiF are present in lower amounts than

S-containing phases, indicating that FSI^- fragments in the SEI do not undergo complete reduction at these cycle conditions.

The next electrolytes comprise a series of conventional carbonates: 1 M $LiPF_6$ EC/DEC + 10 vol% VC (CE = 89.9%); and the same without additive (CE = 92.6%) or with 10 vol% FEC (CE = 95.1%). All have marked presence of semi-carbonate phases, as expected.[37] However, increasing CE corresponds to increasing preponderance of Li_2O, from being nearly comparable to semi-carbonates for the VC-based electrolyte (7.0% of total loss) to well-exceeding semi-carbonates with FEC (26.4%). With fluorinated $LiPF_6$, Li_2O can only originate from solvent-derived phases like semicarbonates[38] and oligo/polycarbonates from either EC, VC or FEC.[39] Reasonably, LiF content was highest with FEC.

Electrolytes with higher CE (generally > 90%) exhibit SEI increasingly dominated by Li_2O. In 1.2 M $LiBF_4$ and 0.6 M $LiBF_4$/0.6 M LiDFOB in 1FEC/2DEC (CE = 95.9% and 97.3%, respectively), Li_2O is followed by significant B-containing phases (**Supplementary Figs. 31–32**) and LiF resulting from salt and FEC breakdown. Meanwhile, the LHCE 1.37 M LiFSI 7TTE/3DMC (CE = 98.6%) has a more chemically-diverse SEI[40] with significant contributions from S-containing phases (*e.g.*, R-SO_2F, **Supplementary Fig. 33**), followed by Li_2O/LiF and more minor contributions of semi-carbonates and Li_3N.

Finally, an electrolyte containing $LiNO_3$ additive was examined (1 M LiTFSI DOL/DME + 3wt% $LiNO_3$, CE = 98.75%). This electrolyte yielded SEI capacity losses overwhelmingly dominated by Li_2O.[27,41] Notably, this electrolyte's cumulative quantification exceeded 100% of capacity loss when normalized to charge measured by the potentiostat. This scenario indicates an SEI-forming contribution from an already partly-reduced anion fragment, here NO_3^-, that decreases the number of electrons consumed to form the SEI Li^+ phases (**Supplementary Note 3**). Across all electrolytes with N-containing salts (LiTFSI, LiFSI without NO_3^-), this electrolyte exhibited the highest amount of fully-reduced Li_3N (4.8%) from extensive anion fragmentation. Together, the above results provide substantial new resolution to SEI composition, enabling further scrutiny of compositional correlations with CE.

Statistical correlations among SEI phases and CE

The relationship of a given phase with CE is generally not monotonic (**Supplementary Fig. 35**). To rigorously identify statistical correlations within the data set, the Spearman rank correlation coefficient (ρ) was utilized.[42] Electrolytes were ranked in order of increasing CE and in proportion of each phase (%), and ρ is the linear coefficient of correlation between ranks (Fig. 3a, **Supplementary Fig. 36**), with ρ = 1/-1/0 for strictly positive/negative/neutral correlations. Associated with each ρ, a degree of statistical significance σ quantifies the null hypothesis probability that an observed correlation could have originated by chance from uncorrelated variables (σ > 2.5 corresponds to < 1%; Fig. 3b and **Supplementary Methods**).

Expectedly,[8] a clear inverse relationship between CE and inactive Li^0 was confirmed (Fig. 3a-b, ρ = −0.818, σ = 2.77), whereas LiF exhibited a positive correlation with CE (ρ = 0.758, σ = 2.42). However, LiF was secondary to Li_2O, which showed the strongest and most statistically significant correlation across all phases (ρ = 0.903, σ = 3.29). When re-evaluating based only on SEI rather than total capacity loss partitioning (**Supplementary Fig. 24**), Li_2O remains the most correlated with CE, but the positive correlation of LiF became even less significant (**Supplementary Figs. 37–38**). All other SEI phases showed yet-weaker statistical significance for CE (σ < 1, Fig. 3b). However, it is emphasized that Li_3N, P-, S- and B-containing phases could not be as rigorously examined because the electrolytes considered do not uniformly span all elemental diversity equally, leading to wide confidence intervals in ρ for these phases (Fig. 3c). Regardless, excepting S-containing phases, these were not typically seen to be major SEI components, and none (including S) were required to achieve high CE, unlike Li_2O. Similarly, the remaining solvent-derived phases, RLi, $ROCO_2Li$ and Li_2C_2, showed weak correlation with CE and wide confidence intervals.

To further test the relationship between Li_2O and CE, Li_2O was measured for four additional lower-CE and four other > 99% CE electrolytes selected from **Supplementary Fig. 1**.[43–46] Fig. 3d shows the CE *vs.* Li_2O relationship for each cycled cell (in grey) and, in yellow, the Li_2O and CE per electrolyte, averaged over at least 3 cells per electrolyte. The rank correlation over all cells (Fig. 3e) confirms the high coefficient of correlation between CE and Li_2O (ρ = 0.88), but now with even stronger statistical significance (σ = 3.7).

Li_2O microstructure within the SEI

Titration-based correlations capture the ensemble composition of the SEI, but deciphering the role of Li_2O in improving CE requires closer scrutiny of distribution and function in the SEI. Cryo-HRTEM was leveraged to localize crystalline phases in low- (1.37 M LiTFSI 7TTE/3DMC) and high-CE (1.37 M LiFSI 7TTE/3DMC, 1 M LiTFSI DOL/DME + 3wt% $LiNO_3$) SEIs from the prior data set (Fig. 4). These experiments were first conducted at low capacity (0.1 mAh/cm^2) to ensure samples remained electron-transparent, and showed varied Li morphology, from needle-like to faceted to oblate respectively, in order of increasing CE (Fig. 4a). All particles were coated by a thin ~ 5–30 nm SEI (Fig. 4b), on which further characterization was performed by selective area electron diffraction (SAED) and energy dispersive spectroscopy (EDS). SAED revealed diffraction rings attributed to Li_2O exclusively, and notably no LiF reflections were found in any electrolyte at this plated capacity (Fig. 4c). However, F-, N- and S-containing phases were detected on all samples by EDS (**Supplementary Fig. 39**), consistent with titration (Fig. 2), thus indicating that the chemically-diverse phases seen by these techniques are amorphous at this plated capacity. HRTEM revealed Li_2O particles in all samples, but with notably distinct spatial distribution between the low- and high-CE SEIs (Fig. 4d). In the two high-CE electrolytes, a uniform ~ 10 nm Li_2O layer was found in all samples, oriented parallel to the SEI surface, consistent with a multilayer SEI nanostructure.[47] Between the outer Li_2O layer and the metallic Li core, additional randomly-oriented crystalline lattices were found within an amorphous SEI matrix. In the low-CE electrolyte, a mosaic-like SEI

nanostructure[48] was observed, with Li_2O particles dispersed heterogeneously within the amorphous SEI matrix.

Altogether, these data suggest that Li_2O-enriched SEIs benefit from the formation of a thick Li_2O outer layer. Indeed, prior work has shown that multilayer SEIs layers facilitate uniform Li stripping compared to mosaic-type SEIs, leading to higher CE and less inactive Li^0.[49] Additionally, a thick and uniform outer layer can inhibit solvent infiltration into the SEI and protect metallic Li from continuous corrosion.[50,51] Thus, the benefits imparted to the SEI by high Li_2O content derive from its distribution and function in the SEI.

To better understand the role played by SEI fluorination, further imaging was conducted on the LHCE 1.37 M LiFSI 7TTE/3DMC electrolyte. At a higher capacity (0.2 mAh/cm^2), the Li morphology changed from faceted to a high aspect ratio deposit (Fig. 4e), and the SEI showed evidence of emerging crystalline LiF superposed with Li_2O. SAED and Fourier transform analysis of the HRTEM image exhibited a reflection around ~ 2 Å (Fig. 4f-h), which can be attributed to LiF{200}. This delayed onset of LiF formation during Li deposition shows an interesting chemical dynamic of SEI formation: the FSI^- anion decomposes to form Li_2O as the earliest and predominant crystalline phase, while other phases containing F, S and N from the FSI^- anion remain amorphous in the SEI matrix and are only later reduced and crystallized, possibly due to contact with subsequently plated Li^0 through the Li_2O-dominant SEI. These findings were further verified by ^{19}F-NMR, which showed a greater abundance of SO_2F-fragments at low capacity compared to LiF, the amounts of which shifted once more Li was plated (Fig. 4i, **Supplementary Fig. 40–42**). Thus, while LiF is a byproduct of SEI evolution during Li plating, the initial SEI formation and morphology evolution of Li are governed primarily by organofluorine and, most significantly, readily-formed Li_2O.

Li_2O formation in localized high concentration electrolytes (LHCE)

To further interrogate the role of Li_2O, an electrolyte series based on LiFSI 7TTE/3DMC was examined as a function of salt concentration, spanning below (0.25 M – 1.25 M) and up to (1.37 M) the LHCE threshold. LiFSI is the most widely used salt in high-CE electrolytes (**Supplementary Fig. 1**), where the higher salt concentrations drive enhanced Li^+-FSI^- pairing, confirmed here *via* DOSY-NMR (Fig. 5a), that promote anion-derived SEI important for high CE.[40,52,53] The first cycle CEs (4 mAh/cm^2, 0.5 mA/cm^2) are shown in Fig. 5b.

Capacity loss breakdowns found Li^0 to be the major contributor at lower CE (16.5–91.4%, 0.25–0.75 M, **Supplementary Fig. 43**). Beyond 0.75 M, CE increases to > 97%, coinciding with a significant increase in Li_2O, and, more modestly, LiF (Fig. 5c). At 1.37 M a substantial increase in R-SO_2F is seen by ^{19}F-NMR along with a suppression in CF_x fragments from TTE decomposition (Fig. 5d, **Supplementary Fig. 44**), thus providing conclusive evidence that LiF derives primarily from anions in this regime. Li_2O can in

principle form from DMC, though because $ROCO_2Li$ (~ 3%) is much lower than Li_2O (~ 25%), a more plausible pathway involves defluorination of LiFSI into LiF, leaving behind NSO_2-like fragments to be further reduced into Li_2O.[54] Relatively little Li_3N was observed, indicating that reduction of the central N occurs less readily than LiF/Li_2O formation. These results reveal that the high CE of LiFSI-based LHCEs is explained by the salt's promotion of Li_2O as the key ionic phase resulting from promoted anion reactivity, significantly moreso than LiF. If true, other salts forming Li_2O could in principle perform an equivalent function, relaxing sole reliance on LiFSI for LHCEs.

To test this hypothesis, we designed an additional series of electrolytes to modulate Li_2O and LiF proportions beyond those achievable with LiFSI (**Fig. 6**). The recipe for LHCE preparation described by Ren *et al.*[40] was adapted, starting with a fixed 3:1 molar ratio of diluent:salt and adding DME until full salt dissolution, to produce LHCEs with selective F– or O–enrichment. TTE/DME electrolytes with O-free salts (1.52 M $LiBF_4$ or 1.57 M $LiPF_6$) yielded poor CE (~ 65% and ~ 91%, respectively, **Fig. 6a-b**), low Li_2O (**Fig. 6c**), and greater amounts of LiF. On the other hand, LHCEs based on $LiClO_4$, *i.e.* an F-free salt, achieved higher CEs between 98.7–99.1% and formed a larger amount of Li_2O (**Fig. 6c**), including an entirely F-free electrolyte with anisole/DME (98.9%) and two with $LiNO_3$ additive (99.1%). The latter represent, to the best of our knowledge, the first electrolytes with fluorine-free salt to breach 99% CE. While strongly oxidizing salts like $LiClO_4$ might not be ideal for full Li-ion cells due to safety concerns,[55] these results indicate that electrolytes yielding Li_2O-rich, LiF-free interphases represent a promising alternative to LiFSI-based LHCEs, which were measured here to have CE = ~ 99.3% (**Fig. 6a-b, Supplementary Fig. 45**), but that are often corrosive and toxic due to their high fluorine content.

Thus, despite LiF being widely regarded as the major desirable SEI phase, high LiF content is not essential for achieving high CE with Li anodes. Such observation is not true for Li_2O: no examined electrolyte in this study could achieve high CE without having Li_2O as the major SEI phase. These findings highlight Li_2O content as a powerful SEI-focused descriptor to guide broad electrolyte discovery, contrasting with existing electrolyte-focused descriptors[16,24,25,52,56-59] that are effective when utilizing LiFSI salts, but which have not yet effectively described performance across broader electrolyte classes. Nonetheless, continued efforts are needed to examine the role of insofar invisible SEI phases (*e.g.*, alkoxides, oligo/polymeric phases), as their contribution to high CE cannot yet be commented upon. Similarly, the results cannot exclude the significance of non-LiF fluorinated phases, which were detected by ^{19}F-NMR and may be quantifiable in the future through more specialized NMR experiments. Finally, fluorination is still likely important for full Li-ion cells,[15] as it aides the cathode by preventing Al corrosion and promoting oxidative stability. Future efforts should focus on integrating and balancing beneficial fluorination and oxygenation features to achieve both anodic and cathodic improvements.

Conclusions

A titration methodology was developed to precisely measure total Li_2O content in cycled Li anodes, adding to a growing suite of chemical titrations available for probing Li anode SEI composition. The new titration was combined with acid and water titration schemes, enabling further quantification of LiF, Li_3N, $ROCO_2Li$, Li_2C_2, RLi, P-, S-, and B-containing phases in addition to inactive Li^0 formed during cycling. Li_2O was found to be the most prevalent phase at high CE across a chemically-diverse set of electrolytes. Consistently, statistical analyses on the titration data revealed that Li_2O has the strongest positive correlation with CE with a correlation coefficient of $\rho > 0.9$, even exceeding that of the broadly regarded LiF ($\rho = 0.758$), countering the prevailing wisdom that LiF is the most important SEI building block. Cryo-TEM analyses showed the significance of the morphology of Li_2O nanostructures, where in low-CE electrolytes Li_2O forms with seemingly-arbitrary crystal planes, contrasting with the highly-organized particles found at high CE that are oriented along the SEI interface and often enveloped in amorphous matrixes. LiFSI, the current leading salt in modern electrolyte design, was shown to be a major driver of Li_2O formation, especially in systems where contact-ion pairing is promoted. Finally, the critical role of Li_2O *vs.* LiF was leveraged to create a first set of completely fluorine-free, oxygen-rich electrolytes to breach 99% CE. This insofar-neglected strategy of SEI oxygenation opens an unexplored design space for high-CE electrolytes, enabling an alternative route beyond fluorination. Such a route is becoming increasingly important as industry seeks to move beyond costly, toxic fluorination schemes which governed the past decades of electrolyte development towards more sustainable paradigms for future battery designs.

Experimental methods

Cell assembly & cycling

Coin cell components (CR2032, MTI) were cleaned with ethanol and DI water, then dried in the vacuum oven at 70°C for at least 12 hours and taken inside an Ar glovebox (MBraun, < 0.1 ppm H_2O, < 0.1 ppm O_2) without ambient exposure. Cu foil current collectors (15 mm diameter) were soaked in 1 M HCl for 1 hour, rinsed with DI water, and similarly dried in a vacuum glass oven at 70°C. Polymeric separators (typically Celgard 2325; 3501 used for 1 M $LiClO_4$ PC due to electrolyte wetting) were punched to 20 mm and were similarly dried and transferred. Lithium foil disks (Alfa Aesar) were punched to 15 mm inside of the glovebox. Each cell was prepared with a total of 50 of L of electrolyte (25 L added before each separator). After assembly, cells were sealed using an automatic crimper (MTI, 0.82 T load setting). The assembled cells were then taken outside of the glovebox, rested for 5 hours at OCV, and cycled galvanostatically at room temperature in a battery cycler (BCS, MTI) for a number of cycles determined by the target capacity loss amounts (see **Supplementary Methods**), with a stripping cut-off voltage of 1 V. Between each plating or stripping half-cycle, the cells rested for 5 minutes at OCV.

Sample preparation and titration

After cycling, cells were taken inside of the glovebox and unsealed using an automated decrimper (MTI). The cycled Cu current collector containing Li^0/SEI residuals was carefully extracted from the cell and prepared according to the type of reactant used for titration. For acid/water titration, samples were soaked in anhydrous DME or DMC for 3 min before the reaction to remove excess electrolyte (**Supplementary Fig. 8**), dried under antechamber vacuum and taken outside of the glovebox in gas-tight vials. For Li_2O quantification, 2-butoxyethanol was used for titration, and no rinsing was required. For LiF, P-containing phases and Li_3N quantification, H_2O was used for titration. For Li^0, $ROCO_2Li$, Li_2C_2, RLi, S-containing, and B-containing phases, 3.5 M HCl was used for titration. See **Supplementary Methods** for detailed information on each analytical technique, their appropriate calibrations and sensitivities.

For HCl titration, 500 µL of 3.5 M HCl was injected into the vial using a gas-tight syringe. After > 8 hours, 2.5 mL of gas were extracted from the headspace of the vial and injected into a GC (Agilent 7890A) to quantify the amounts of H_2, CO_2, C_2H_2, CH_4, C_2H_6, C_2H_4, which determine the total amount of Li^0, $ROCO_2Li$, Li_2C_2 and RLi. The vial was opened and another 500 µL of DI water was added, further diluting the liquid solution in a total volume of 1 mL. Using the resulting solution, samples were then prepared for ICP analysis to determine the concentration of S- and B- containing phases in solution. The acid titration scheme is depicted in **Supplementary Fig. 5**.

For H_2O titration, 500 µL of DI H_2O was injected into the vial using a gas-tight syringe. After > 8 hours, 2.5 mL of gas were extracted from the headspace of the vial using a gas-tight syringe, and injected into the GC for analysis (see Methods). Then, the vial was opened and another 1 mL of DI water, further diluting the liquid solution in a total volume of 1.5 mL. Using the resulting solution, samples were then prepared for ^{19}F-NMR to determine the concentration of LiF, for ICP-AES to determine the concentration of P-containing phases, and for UV-Vis analysis to determine the concentration of Li_3N following a salicylate assay.[35] The water titration scheme is depicted in **Supplementary Fig. 6**.

For 2-butoxyethanol titration, special care was taken to further suppress contamination from water of the materials used in the analysis. As such, after regular vacuum drying at 70°C, all materials and utensils, including vials, tweezers, syringes and needles, were dried in a vacuum glass oven at 70°C for at least 12 hours, and taken inside of the glovebox without any atmospheric exposure. Inside of the glovebox, the cycled Cu current collector and the separator closest to it were carefully extracted from the cell and closed inside a dry gas-tight vial without rinsing. Immediately after, 500 µL of dry butoxyethanol (typically ~ 3 ppm H_2O) was injected into the vial through a septum using a dry gas-tight syringe. After ~ 24 hours, when the sample had fully reacted, another 1.5 mL of butoxyethanol was added to the vial, resulting in a 2 mL solution per sample. The solution was then analyzed by KF titration to determine the concentration of Li_2O in the solution. The 2-butoxyethanol titration scheme is depicted in **Supplementary Fig. 7**.

Coulometric Karl-Fischer (KF) titration of Li_2O

Upon reaction of the Li residuals with 2-butoxyethanol, Li_2O was converted into LiOH following the reaction ROH + Li_2O → LiOH + ROLi (R = $CH_3(CH_2)_3O(CH_2)_2$ for 2-butoxyethanol). The KF electrolyte (CombiCoulomat fritless) is methanol-based and contains a small amount of hydroiodic acid (HI) due to the presence of iodine (I_2) in the solution, which is needed for KF titration. When added to the electrolyte, the hydroxide in the sample solution is consumed by HI, forming water stoichiometrically (LiOH + HI → H_2O + LiI), which then follows the typical Karl-Fischer reaction by consuming iodine ($H_2O + I_2 + SO_2$ + 3 RN + CH_3OH → 2 RN HI + RN HSO_4CH_3). Iodine is then rebalanced coulometrically by the generator electrode in the KF titrator, and the charge needed for rebalancing is recorded ($2\ I^+ + 2\ e^- \rightarrow I_2$). Hence, there is a direct and stoichiometric relationship between the original amount of Li_2O in the sample and the charge measured for rebalancing iodine ($2\ e^-_{KF} = 1\ Li_2O$), as shown in Fig. 1b. More details on KF titration in **Supplementary Methods**.

Cryogenic transmission electron microscopy (Cryo-TEM)

Cu/Li cells used for Cryo-TEM were assembled as usual, with the only difference being the addition of 3 TEM Cu grids (Ted Pella, 1GC300) directly on top of the Cu current collector. Li was directly plated on the TEM grids at 0.5 mA/cm^2 to a capacity of either 0.1 or 0.2 mAh/cm^2 and immediately taken inside of the glovebox and disassembled for analysis. After disassembly, the grids were carefully rinsed by droplets of DMC or DME based on the solvent of the electrolyte, and subsequently grids were placed on a piece of Kimwipe in the glovebox for ten minutes to dry out the remaining rinsing solvents, then grids were sealed in Eppendorf tubes separately with Parafilm to ensure air-tight transfer. Afterwards, the Eppendorf tubes with grids inside were transferred outside of the glovebox and immediately immersed in a Styrofoam container filled with liquid nitrogen and the Eppendorf tubes were crushed by a pair of pliers to make the grids immersed in the LN2. Grids were transferred into a grid box within LN2 and then stored in a Dewar for following cryo analysis.

Cryo analysis was conducted by an instrument in the EICN (Electron Imaging Center for Nanomachines) at CNSI (California NanoSystems Institute), using a FEI Titan 80–300 scanning transmission electron microscope operated at an accelerating voltage of 300 kV, which is equipped with a field emission gun, an Oxford X-MaxTEM 100N TLE windowless SDD 100 mm^2 for EDS and Ultrascan US1000 1K digital camera. The grids were transferred into the TEM column with Gatan 626 cryo-transfer holder and the grids were immersed in LN2 during the whole transfer process to avoid potential air contamination. After insertion of the cryo holder, the temperature was maintained at -178°C. The electron flux under low magnification was around 100 $e \cdot Å^{-2} \cdot s^{-1}$ and 1000 $e \cdot Å^{-2} \cdot s^{-1}$ under high magnification. The acquisition time for SAED images was 0.05 s and for TEM images was 0.4 to 2 s.

Declarations

Supporting Information

Contains additional experimental methods, supporting analyses, figures and tables.

Acknowledgements

This work made use of the MIT Materials Research Science and Engineering Center Shared Experimental Facilities, supported by the National Science Foundation under award number DMR-14-19807. This work also made use of the MIT Department of Chemistry Instrumentation Facility. The cryo-EM work was supported by the U.S. Department of Energy, Office of Science, Office of Basic Energy Sciences, under Award Number DE-SC0022955. We also thank Prof. Tonio Buonassisi, MIT, for helpful discussions regarding the statistical analysis presented herein.

References

1. Adams, B. D., Zheng, J., Ren, X., Xu, W. & Zhang, J. G. Accurate Determination of Coulombic Efficiency for Lithium Metal Anodes and Lithium Metal Batteries. *Adv. Energy Mater.* **8**, 1702097 (2017).
2. Electrochemical Energy Storage Technical Team Roadmap. (Vehicle Technologies Office, 2017).
3. Schmuch, R., Wagner, R., Hörpel, G., Placke, T. & Winter, M. Performance and Cost of Materials for Lithium-Based Rechargeable Automotive Batteries. *Nat. Energy* **3**, 267-278 (2018).
4. Batteries: 2021 Annual Progress Report. (Vehicle Technologies Office, 2022).
5. Xiao, J. *et al.* Understanding and Applying Coulombic Efficiency in Lithium Metal Batteries. *Nat. Energy* **5**, 561-568 (2020).
6. Hobold, G. M. *et al.* Moving Beyond 99.9% Coulombic Efficiency for Lithium Anodes in Liquid Electrolytes. *Nat. Energy* **6**, 951-960 (2021).
7. Hobold, G. M. & Gallant, B. M. Quantifying Capacity Loss Mechanisms of Li Metal Anodes Beyond Inactive Li^0. *ACS Energy Lett.* **7**, 3458-3466 (2022).
8. Fang, C. *et al.* Quantifying Inactive Lithium in Lithium Metal Batteries. *Nature* **572**, 511-515 (2019).
9. Meng, Y. S., Srinivasan, V. & Xu, K. Designing Better Electrolytes. *Science* **378**, eabq3750 (2022).
10. Wu, H., Jia, H., Wang, C., Zhang, J. G. & Xu, W. Recent Progress in Understanding Solid Electrolyte Interphase on Lithium Metal Anodes. *Adv. Energy Mater.* **11**, 2003092 (2020).
11. Peled, E. & Menkin, S. Review—SEI: Past, Present and Future. *J. Electrochem. Soc.* **164**, A1703-A1719 (2017).
12. Yu, W., Yu, Z., Cui, Y. & Bao, Z. Degradation and Speciation of Li Salts During XPS Analysis for Battery Research. *ACS Energy Lett.* **7**, 3270-3275 (2022).
13. Dedryvère, R. *et al.* XPS Identification of the Organic and Inorganic Components of the Electrode/Electrolyte Interface Formed on a Metallic Cathode. *J. Electrochem. Soc.* **152**, A689 (2005).
14. Schechter, A., Aurbach, D. & Cohen, H. X-Ray Photoelectron Spectroscopy Study of Surface Films Formed on Li Electrodes Freshly Prepared in Alkyl Carbonate Solutions. *Langmuir* **15**, 3334-3342 (1999).

15. Wang, C., Meng, Y. S. & Xu, K. Perspective—Fluorinating Interphases. *J. Electrochem. Soc.* **166**, A5184-A5186 (2018).
16. Suo, L. *et al.* Fluorine-Donating Electrolytes Enable Highly Reversible 5-V-Class Li Metal Batteries. *Proc. Natl. Acad. Sci. U. S. A.* **115**, 1156-1161 (2018).
17. Tan, J., Matz, J., Dong, P., Shen, J. & Ye, M. A Growing Appreciation for the Role of LiF in the Solid Electrolyte Interphase. *Adv. Energy Mater.* **11**, 2100046 (2021).
18. Li, T., Zhang, X.-Q., Shi, P. & Zhang, Q. Fluorinated Solid-Electrolyte Interphase in High-Voltage Lithium Metal Batteries. *Joule* **3**, 2647-2661 (2019).
19. Guo, R. & Gallant, B. M. Li_2O Solid Electrolyte Interphase: Probing Transport Properties at the Chemical Potential of Lithium. *Chem. Mater.* **32**, 5525-5533 (2020).
20. Smeu, M. & Leung, K. Electron Leakage through Heterogeneous LiF on Lithium-Metal Battery Anodes. *Phys. Chem. Chem. Phys.* **23**, 3214-3218 (2021).
21. Chen, Y. C., Ouyang, C. Y., Song, L. J. & Sun, Z. L. Electrical and Lithium Ion Dynamics in Three Main Components of Solid Electrolyte Interphase from Density Functional Theory Study. *J. Phys. Chem. C* **115**, 7044-7049 (2011).
22. He, M., Guo, R., Hobold, G. M., Gao, H. & Gallant, B. M. The Intrinsic Behavior of Lithium Fluoride in Solid Electrolyte Interphases on Lithium. *Proc. Natl. Acad. Sci. U. S. A.* **117**, 73-79 (2020).
23. Huang, W., Wang, H., Boyle, D. T., Li, Y. & Cui, Y. Resolving Nanoscopic and Mesoscopic Heterogeneity of Fluorinated Species in Battery Solid-Electrolyte Interphases by Cryogenic Electron Microscopy. *ACS Energy Lett.* **5**, 1128-1135 (2020).
24. Zhao, Y. *et al.* Electrolyte Engineering for Highly Inorganic Solid Electrolyte Interphase in High-Performance Lithium Metal Batteries. *Chem* **9**, 682-697 (2023).
25. Yu, Z. *et al.* Rational Solvent Molecule Tuning for High-Performance Lithium Metal Battery Electrolytes. *Nat. Energy* **7**, 94-106 (2022).
26. Kim, M. S. *et al.* Suspension Electrolyte with Modified Li^+ Solvation Environment for Lithium Metal Batteries. *Nat. Mater.* **21**, 445-454 (2022).
27. Liu, Y. *et al.* Solubility-Mediated Sustained Release Enabling Nitrate Additive in Carbonate Electrolytes for Stable Lithium Metal Anode. *Nat. Commun.* **9**, 3656 (2018).
28. Deng, W. *et al.* Quantification of Reversible and Irreversible Lithium in Practical Lithium-Metal Batteries. *Nat. Energy* **7**, 1031-1041 (2022).
29. McShane, E. J. *et al.* Quantifying Graphite Solid-Electrolyte Interphase Chemistry and Its Impact on Fast Charging. *ACS Energy Lett.* **7**, 2734-2744 (2022).
30. Xiang, Y. *et al.* Quantitatively Analyzing the Failure Processes of Rechargeable Li Metal Batteries. *Sci. Adv.* **7**, eabj3423.
31. von Holtum, B. *et al.* Accessing the Primary Solid-Electrolyte Interphase on Lithium Metal: A Method for Low-Concentration Compound Analysis. *ChemSusChem* **16**, e202201912 (2023).

32. Jaworowski, R. J., Potts, J. R. & Hobart, E. W. The Determination of Oxygen in Lithium. *Anal. Chem.* **35**, 1275-1279 (1963).
33. Sax, H. I. & Steinmetz, H. Determination of Oxygen in Lithium Metal. (Oak Ridge National Laboratory, United States, 1958).
34. Lu, J. *et al.* A Lithium-Oxygen Battery Based on Lithium Superoxide. *Nature* **529**, 377-382 (2016).
35. Steinberg, K. *et al.* Imaging of Nitrogen Fixation at Lithium Solid Electrolyte Interphases Via Cryo-Electron Microscopy. *Nat. Energy* **8**, 138-148 (2022).
36. Fiedler, C., Luerssen, B., Rohnke, M., Sann, J. & Janek, J. XPS and SIMS Analysis of Solid Electrolyte Interphases on Lithium Formed by Ether-Based Electrolytes. *J. Electrochem. Soc.* **164**, A3742-A3749 (2017).
37. Aurbach, D., Ein-Ely, Y. & Zaban, A. The Surface Chemistry of Lithium Electrodes in Alkyl Carbonate Solutions. *J. Electrochem. Soc.* **141**, L1-L3 (2019).
38. Leung, K., Soto, F., Hankins, K., Balbuena, P. B. & Harrison, K. L. Stability of Solid Electrolyte Interphase Components on Lithium Metal and Reactive Anode Material Surfaces. *J. Phys. Chem. C* **120**, 6302-6313 (2016).
39. Michan, A. L. *et al.* Fluoroethylene Carbonate and Vinylene Carbonate Reduction: Understanding Lithium-Ion Battery Electrolyte Additives and Solid Electrolyte Interphase Formation. *Chem. Mater.* **28**, 8149-8159 (2016).
40. Ren, X. *et al.* Role of Inner Solvation Sheath within Salt-Solvent Complexes in Tailoring Electrode/Electrolyte Interphases for Lithium Metal Batteries. *Proc. Natl. Acad. Sci. U. S. A.* **117**, 28603-28613 (2020).
41. Jaumann, T. *et al.* Role of 1,3-Dioxolane and $LiNO_3$ addition on the Long Term Stability of Nanostructured Silicon/Carbon Anodes for Rechargeable Lithium Batteries. *J. Electrochem. Soc.* **163**, A557-A564 (2016).
42. Corder, G. W., Foreman, D. I. Comparing Variables of Ordinal or Dichotomous Scales: Spearman Rank-Order, Point-Biserial, and Biserial Correlations, in *Nonparametric Statistics for Non-Statisticians.* 122-154 (John Wiley & Sons, 2011).
43. Huang, Y. *et al.* Eco-Friendly Electrolytes Via a Robust Bond Design for High-Energy Li Metal Batteries. *Energy Env. Sci.* **15**, 4349-4361 (2022).
44. Liu, S. *et al.* An Inorganic-Rich Solid Electrolyte Interphase for Advanced Lithium-Metal Batteries in Carbonate Electrolytes. *Angew. Chem.* **60**, 3661-3671 (2021).
45. Qiu, F. *et al.* A Concentrated Ternary-Salts Electrolyte for High Reversible Li Metal Battery with Slight Excess Li. *Adv. Energy Mater.* **9**, 1803372 (2018).
46. Wang, Q. *et al.* Interface Chemistry of an Amide Electrolyte for Highly Reversible Lithium Metal Batteries. *Nat. Commun.* **11**, 4188 (2020).
47. Zaban, A., Zinigrad, E. & Aurbach, D. Impedance Spectroscopy of Li Electrodes. 4. A General Simple Model of the Li−Solution Interphase in Polar Aprotic Systems. *J. Phys. Chem.* **100**, 3089-3101

(1996).

48. Peled, E., Golodnitsky, D. & Ardel, G. Advanced Model for Solid Electrolyte Interphase Electrodes in Liquid and Polymer Electrolytes. *J. Electrochem. Soc.* **144**, L208 (1997).
49. Li, Y. *et al.* Correlating Structure and Function of Battery Interphases at Atomic Resolution Using Cryoelectron Microscopy. *Joule* **2**, 2167-2177 (2018).
50. Zhang, Z. *et al.* Capturing the Swelling of Solid-Electrolyte Interphase in Lithium Metal Batteries. *Science* **375**, 66-70 (2022).
51. Boyle, D. T. *et al.* Corrosion of Lithium Metal Anodes During Calendar Ageing and Its Microscopic Origins. *Nat. Energy* **6**, 487-494 (2021).
52. Cao, X., Jia, H., Xu, W. & Zhang, J.-G. Review—Localized High-Concentration Electrolytes for Lithium Batteries. *J. Electrochem. Soc.* **168**, 010522 (2021).
53. Chen, S. *et al.* High-Voltage Lithium-Metal Batteries Enabled by Localized High-Concentration Electrolytes. *Adv. Mater.* **30**, 1706102 (2018).
54. Shkrob, I. A., Marin, T. W., Zhu, Y. & Abraham, D. P. Why Bis(Fluorosulfonyl)Imide Is a “Magic Anion” for Electrochemistry. *J. Phys. Chem. C* **118**, 19661-19671 (2014).
55. Xu, K. Nonaqueous Liquid Electrolytes for Lithium-Based Rechargeable Batteries. *Chem. Rev.* **104**, 4303-4418 (2004).
56. Ko, S. *et al.* Electrode Potential Influences the Reversibility of Lithium-Metal Anodes. *Nat. Energy* **7**, 1217-1224 (2022).
57. Yu, Z. *et al.* Molecular Design for Electrolyte Solvents Enabling Energy-Dense and Long-Cycling Lithium Metal Batteries. *Nat. Energy* **5**, 526-533 (2020).
58. Kim, S. C. *et al.* Data-Driven Electrolyte Design for Lithium Metal Anodes. *Proc. Natl. Acad. Sci. U. S. A.* **120**, e2214357120 (2023).
59. Fan, X. *et al.* Highly Fluorinated Interphases Enable High-Voltage Li-Metal Batteries. *Chem* **4**, 174-185 (2018).

Figures

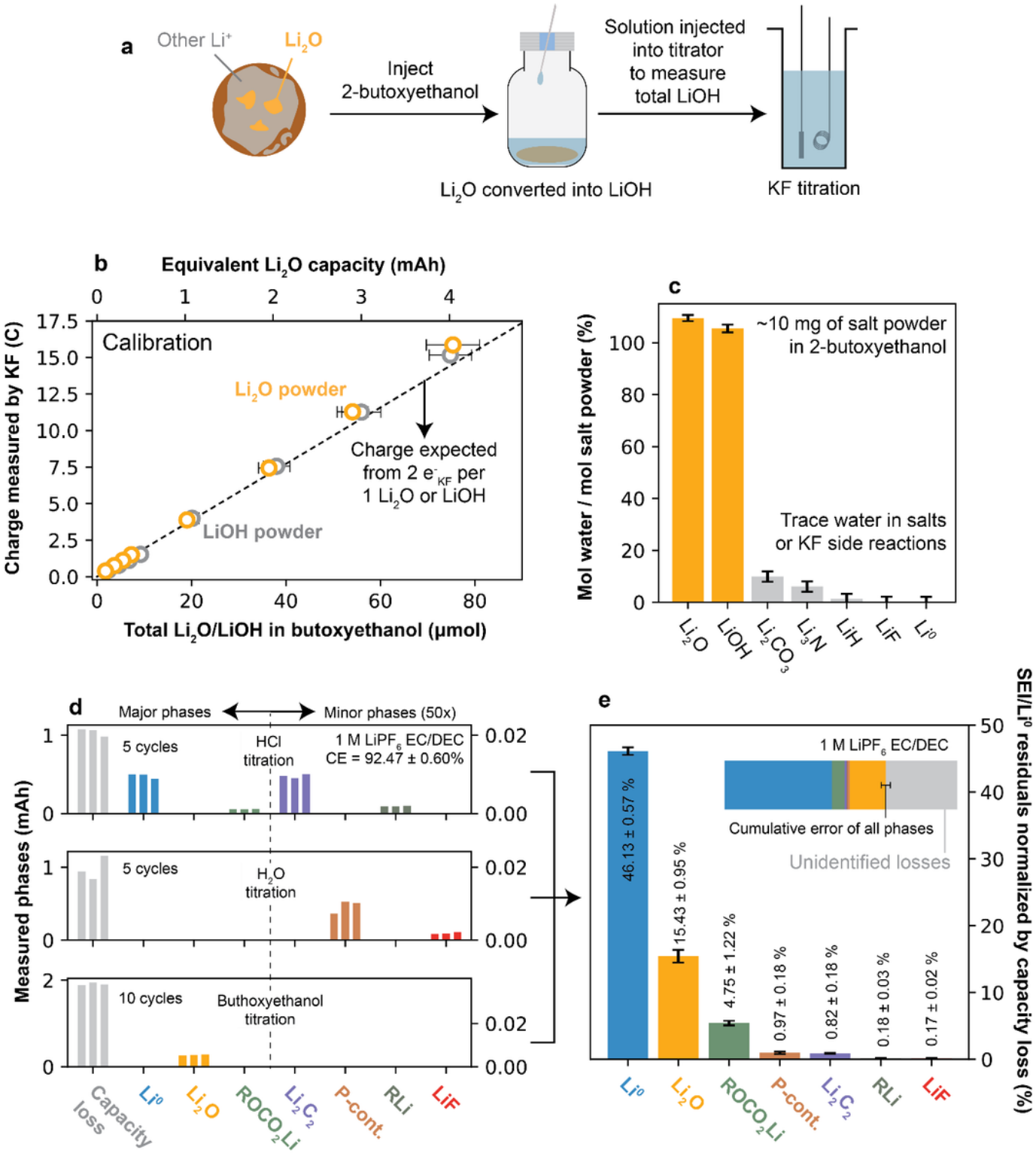

Figure 1

Titration strategy for quantification of Li_2O in cycled Li anodes. (a) Illustration of the experimental workflow used for Li_2O quantification, based on conversion of Li_2O into LiOH by reaction with 2-butoxyethanol, followed by titration of the resulting hydroxide using a coulometric Karl-Fischer (KF) method. **(b)** Charge measured by the coulometric KF method after titration of standard solutions of LiOH

and Li_2O in 2-butoxyethanol. The dashed line confirms the typical expected titrated 2 e^- charge for each Li_2O/LiOH molecule. Slight deviation from the expected value at higher mol values is due to residual water in the powders. **(c)** Sensitivity of the KF method to other SEI phases and Li^0, in which 10 mg of each material were dissolved/reacted with 1 mL of 2-butoxyethanol and subsequently titrated by the KF method after 24 h. **(d)** Capacity loss in the 1 M $LiPF_6$ EC/DEC electrolyte attributed to individual phases, measured after 5-10 full cycles (0.5 mA/cm^2, 1.5 mAh/cm^2), now including Li_2O in addition to the Li^0, $ROCO_2Li$, Li_2C_2, RLi, LiF and P-containing phases. **(e)** Partitioning of the total capacity loss, in which the absolute measured quantities of each phase in (d) are normalized by each cell's measured capacity loss. Error bars denote the standard deviation over at least 3 cells.

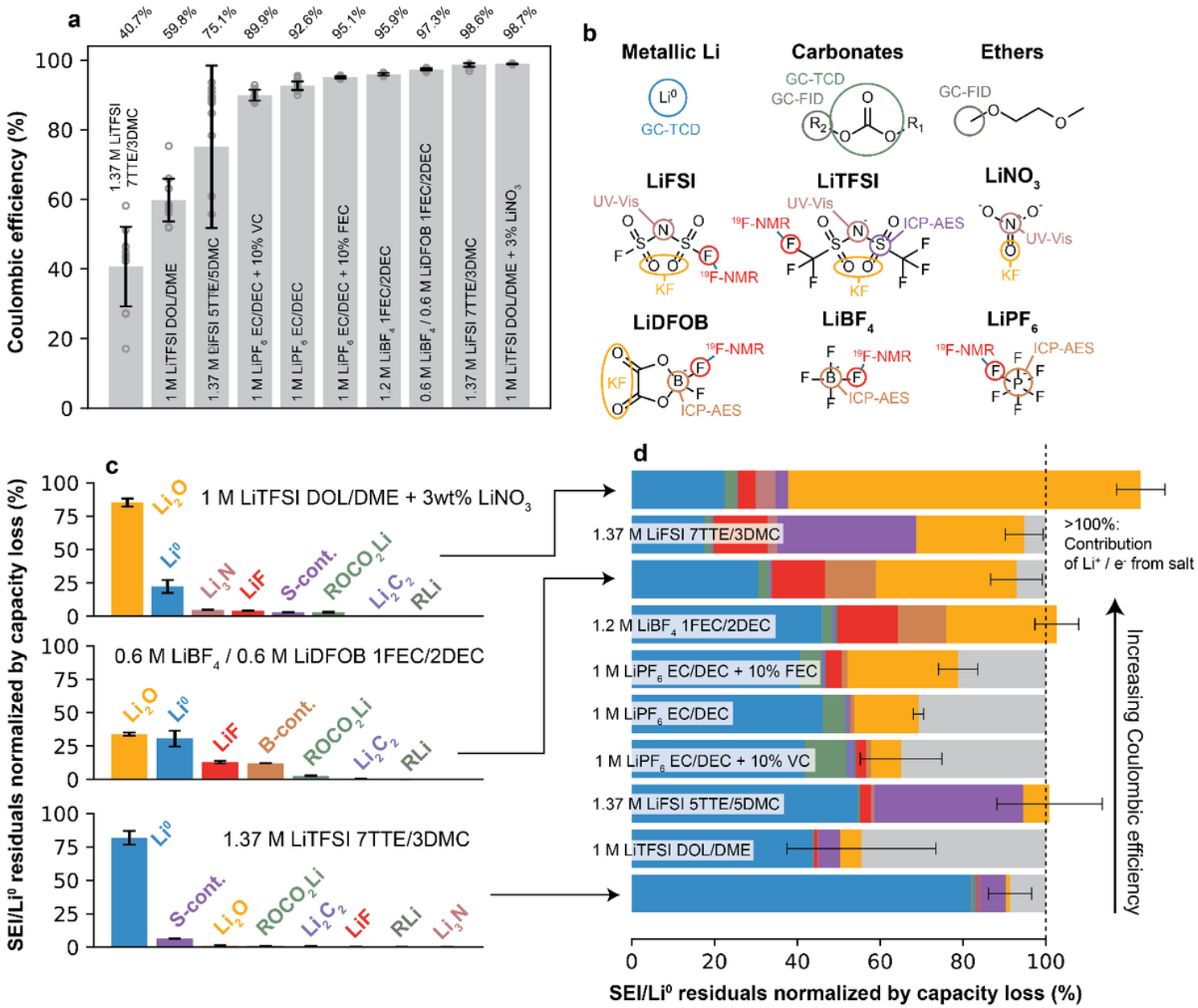

Figure 2

Quantification of SEI/Li^0 residuals in diverse electrolytes. (a) Coulombic efficiency across diverse electrolytes, determined by the same cycling protocol used to generate the titration samples (see **Supplementary Methods**). Results are measured as an average over at least 3 cells upon galvanostatic plating/stripping. Error bars denote the standard deviation and open markers denote individual cells. Lower CE electrolytes consistently displayed larger scatter than high CE electrolytes. **(b)** Examples of solvent species and salts present in the electrolytes considered herein, annotated with the instrument/titration techniques used to measure decomposition products from the indicated chemical moieties. **(c)** Measured SEI/Li^0 residuals normalized by capacity loss for select electrolytes in the series. Error bars denote standard deviation of each phase over at least 3 cells. **(d)** Cumulative SEI/Li^0 residuals normalized by capacity loss for all electrolytes in the series, organized by CE. Colors as in (c). The error bars denote the estimated cumulative error of all phases, calculated from the root square sum of the error bars in (c). In electrolytes for which there is extensive anion decomposition, >100% cumulative Li residuals can occur due to the contribution from charged salt ions to the Li inventory on the cycled electrode (see **Supplementary Note 3** for $LiNO_3$ as an example). **Supplementary Fig. 24** shows the data for the SEI phases (d), but normalized by SEI, rather than total, capacity loss (*i.e.*, total capacity loss minus inactive Li^0).

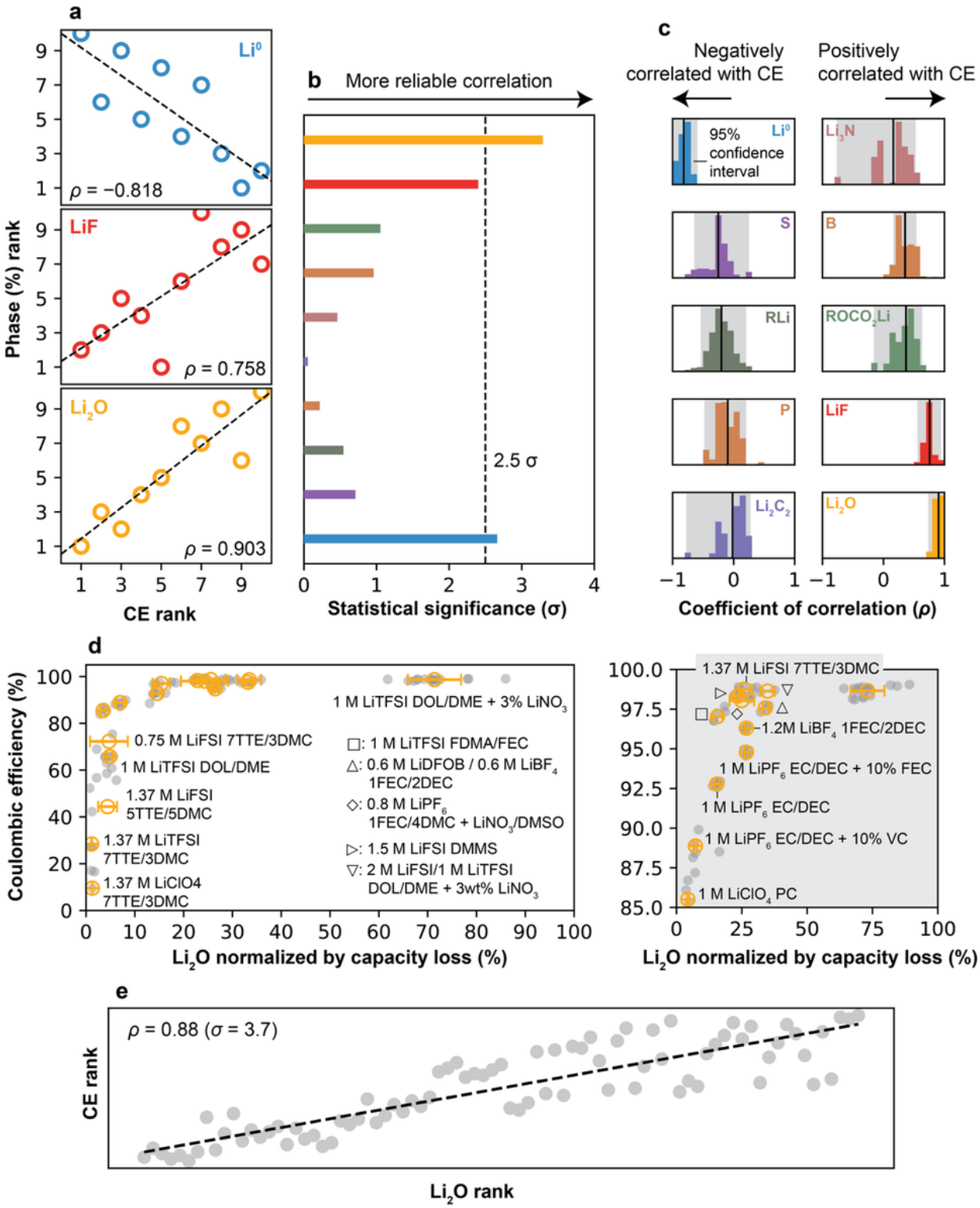

Figure 3

Statistical correlations between quantifiable SEI/Li^0 residual phases and CE. **(a)** Rank CE and rank phase (%) for inactive Li^0, LiF and Li_2O. The coefficient of correlation ρ measures whether the relationship between CE and a given phase is monotonic, with $\rho = 1$ perfectly monotonic and positively correlated, and $\rho = -1$ perfectly monotonic and negatively correlated. Each data point indicates a different electrolyte. **(b)** Statistical significance σ associated with each phase-CE correlation. **(c)** Frequency histograms of ρ,

calculated from all possible combinations of (10 choose 7) data points (*i.e.*, excluding up to 3 data points from the data set). Dashed line indicates ρ calculated from all 10 data points and shaded region indicates the 95% confidence interval calculated from the frequency histogram. **(d)** CE *vs.* Li_2O relationship, now including 8 additional electrolytes (18 total; additional electrolytes are 1.37 M $LiClO_4$ 7TTE/3DMC, 0.5 M and 0.75 M LiFSI 7TTE/3DMC, 1 M $LiClO_4$ PC, 1.5 M LiFSI DMMS, 1 M LiTFSI FDMA/FEC, 0.8 M $LiPF_6$ 1FEC/3DMC + 4 M $LiNO_3$/DMSO and 2 M LiFSI/1 M LiTFSI DOL/DME + 3wt% $LiNO_3$). CE and Li_2O were measured using cycling conditions that meet the capacity loss requirements for 2-butoxyethanol titration. **(e)** Rank correlation from (d).

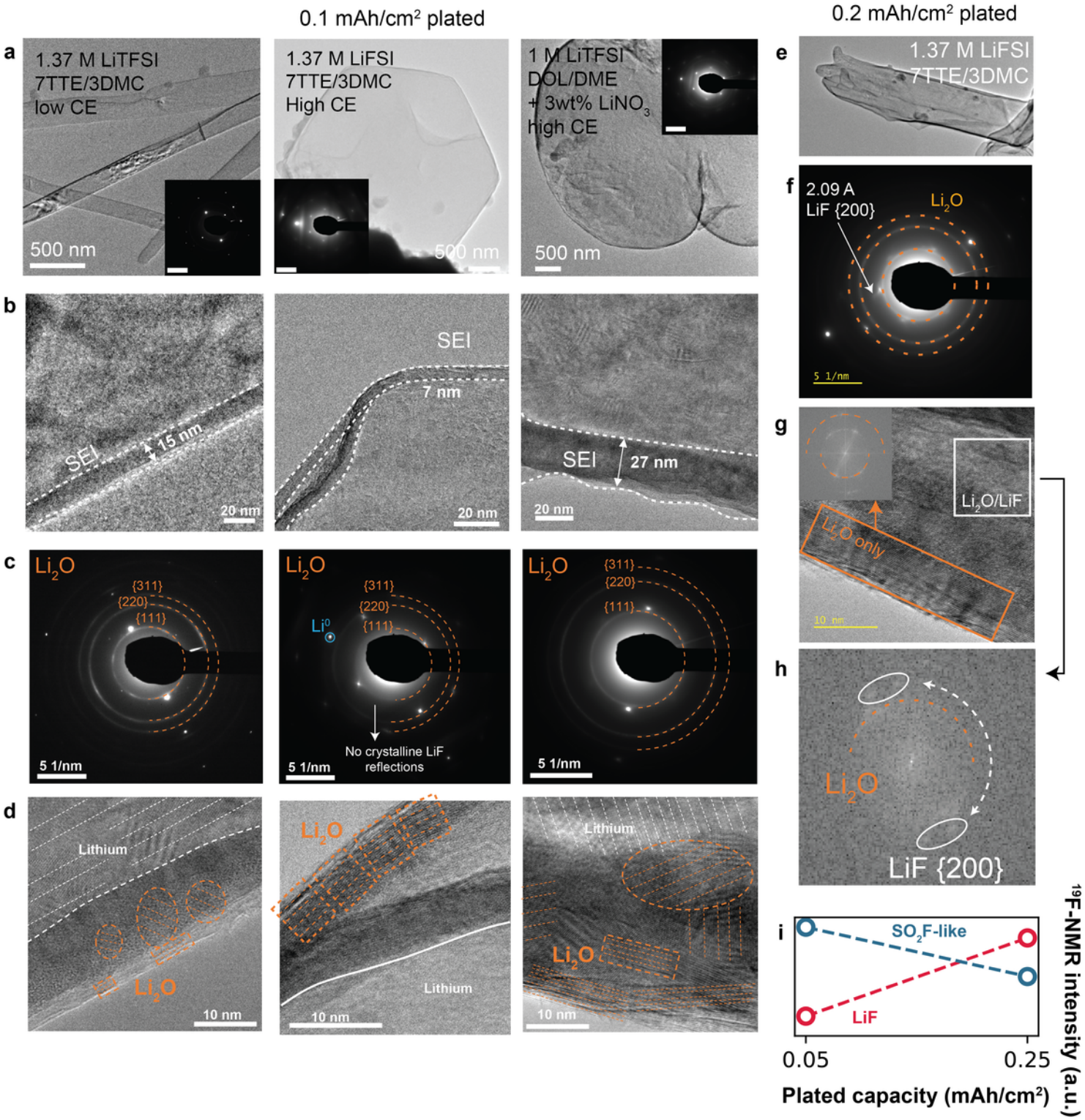

Figure 4

Cryo-TEM imaging of Li_2O in plated Li electrodes. (a) Low magnification images of the plated Li deposit morphology (after 0.1 mAh/cm^2, no stripping) in low- and high-CE electrolytes, chosen from the quantification analysis in **Fig. 2**. **(b)** Magnification of the interface between the Li deposit and vacuum, highlighting the thickness of the SEI. **(c)** SAED measurements near the interface. **(d)** HR-TEM images of the crystalline lattices within the SEI. **(e)** Low magnification image of a Li deposit in the 1.37 M LiFSI

7TTE/3DMC LHCE electrolyte, now at 0.2 mAh/cm^2 plated capacity. **(f)** SAED patterns of the SEI. **(g)** HR-TEM images of the crystalline phases in the SEI. Inner frame indicates the Fourier transform of the outer SEI region with only Li_2O reflections. **(h)** Fourier transform of the white region indicated in (g), with both Li_2O and LiF reflections. **(i)** ^{19}F-NMR measurements of R-SO_2F and LiF in plated Li electrodes.

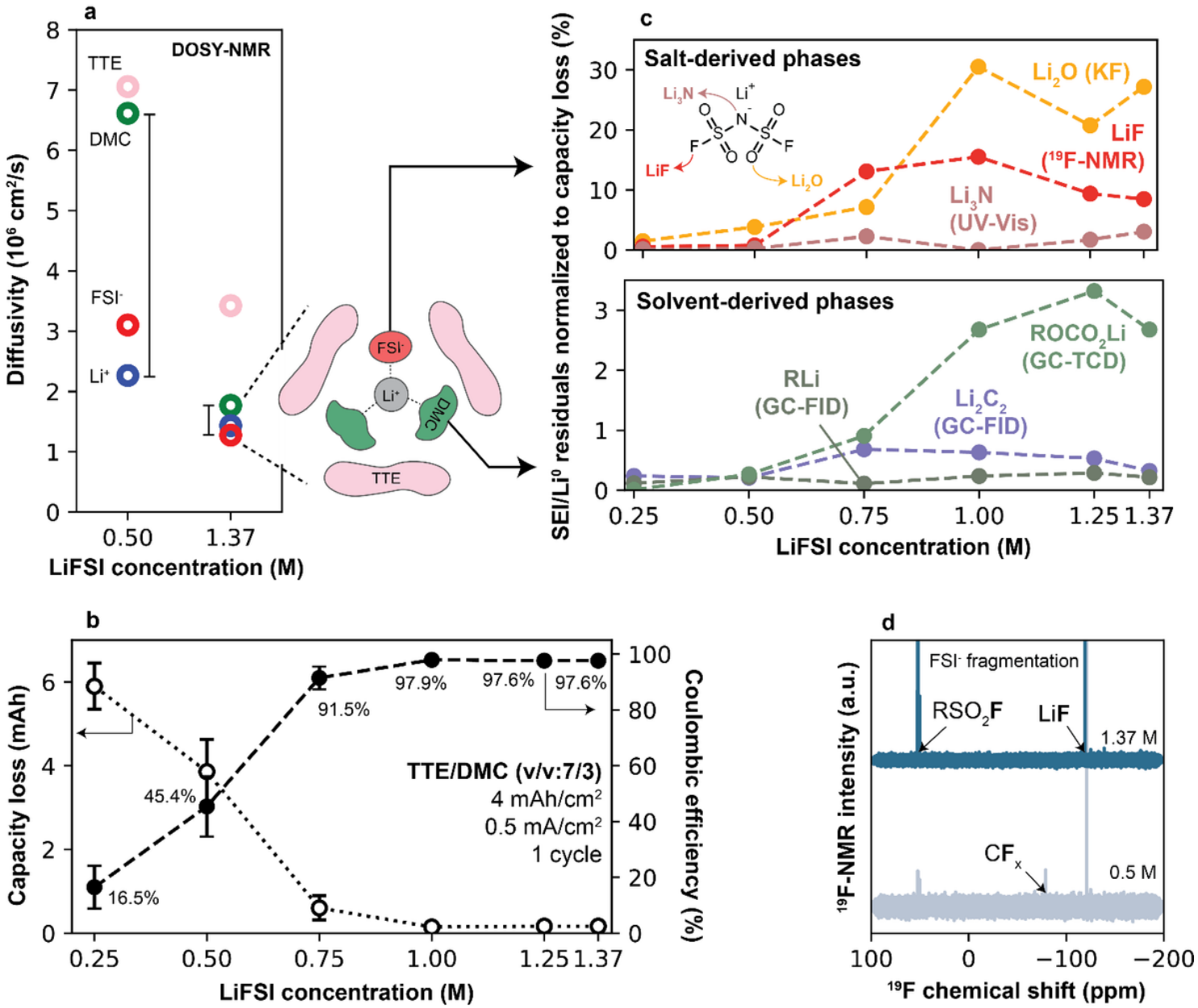

Figure 5

Li_2O formation in LiFSI-based LHCE electrolytes. (a) Diffusivity of all electrolyte components in 0.5 M and 1.37 M LiFSI TTE/DMC measured by DOSY-NMR, revealing the formation of DMC-Li^+-FSI^- coordination shells. **(b)** Capacity loss and CE after the first cycle (4 mAh/cm^2, 0.5 mA/cm^2) in the LHCE-like electrolytes LiFSI 7TTE/3DMC, with salt concentrations increasing from 0.5 M to 1.37 M. **(c)** Salt-derived SEI phases (Li_3N, LiF and Li_2O) and solvent-derived SEI phases ($ROCO_2Li$, Li_2C_2, RLi) normalized to

capacity loss, measured after the first cycle. **(d)** ^{19}F-NMR of electrodes in H_2O after the first cycle in the 0.5 M and 1.37 M LiFSI TTE/DMC electrolytes.

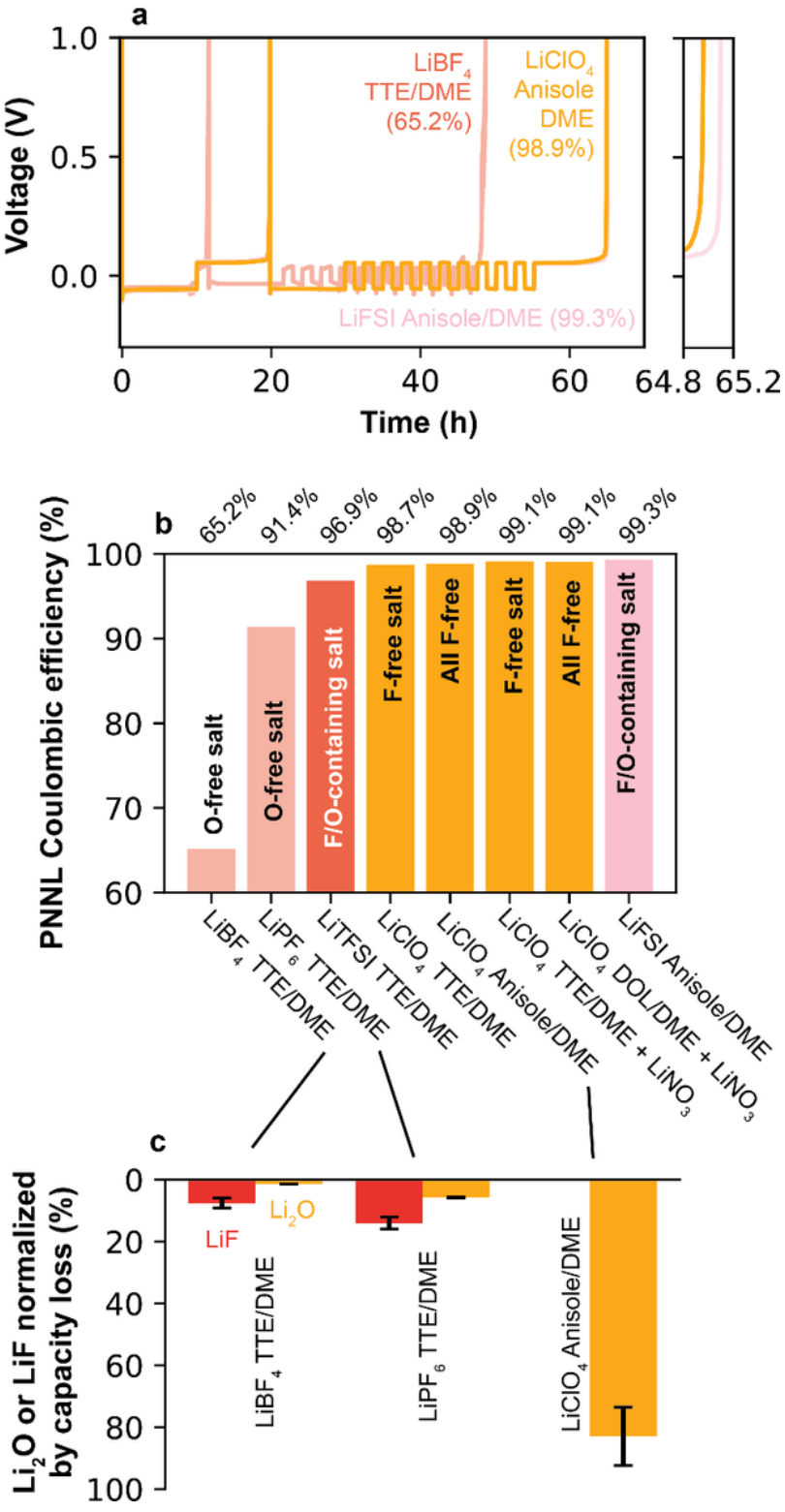

Figure 6

Design of fluorine-free high-CE electrolytes. (a) Cycling data used to measure CE in the LHCEs tested herein (0.4 mA/cm^2, 4 mAh/cm^2 formation cycle, 4 mAh/cm^2 reservoir, 0.5 mAh/cm^2 cycles), following

the PNNL protocol.[1] **(b)** Summary of CEs measured for LHCEs containing $LiBF_4$, $LiPF_6$, LiTFSI, LiFSI, $LiClO_4$ and $LiNO_3$ as salts. **(c)** Total amounts of Li_2O and LiF normalized by capacity loss in select electrolytes. Full electrolyte formulations correspond to, in order of CE: 1.52 M $LiBF_4$ 0.69-TTE/0.31-DME; 1.57 M $LiPF_6$ 0.71-TTE/0.29-DME; 1.64 M LiTFSI 0.74-TTE/0.26-DME; 1.7 M $LiClO_4$ 0.77-TTE/0.23-DME; 2.27 M $LiClO_4$ 0.74-anisole/0.26-DME; 1.7 M $LiClO_4$ 0.77-TTE/0.23-DME + ~0.1 M $LiNO_3$; 1 M $LiClO_4$ DOL/DME + 3wt% $LiNO_3$; 1.56 M LiFSI 0.8-TTE/0.2-DME; solvent fractions given in vol/vol.

Supplementary Files

This is a list of supplementary files associated with this preprint. Click to download.

- SupplementaryInformation.pdf